Usefulness of Textural Analysis as a Tool for Noninvasive Liver Fibrosis Staging

Cristian VICAS, Monica LUPSOR, Radu BADEA, Sergiu NEDEVSCHI
Corresponding author: Cristian VICAS

Cristian VICAS, Automation and Computer Science, Technical University of Cluj-Napoca, Memorandumului Str. No. 28, Cluj-Napoca 400114, Romania
Tel.: +4 0264 401 200, Fax: +4 0264 592 055; cristian.vicas@cs.utcluj.ro

Monica LUPSOR, Department of Ultrasonography, 3rd Medical Clinic, 19 – 21 Croitorilor St., Cluj-Napoca, Romania. monica.lupsor@umfcluj.ro

Radu BADEA, Department of Ultrasonography, 3rd Medical Clinic, 19 – 21 Croitorilor St., Cluj-Napoca, Romania. rbadea@umfcluj.ro

Sergiu NEDEVSCHI , Automation and Computer Science, Technical University of Cluj-Napoca, Memorandumului Str. No. 28, Cluj-Napoca 400114, Romania. sergiu.nedevschi@cs.utcluj.ro

Accepted: 2010/08/06
Received: 2011/03/28

Abstract
Purpose – Noninvasive diagnosis of liver fibrosis is a popular topic in the medical literature. Textural analysis on B-mode ultrasound is viewed as a noninvasive tool for fibrosis staging. A liver tissue model is proposed and used to simulate ultrasound images.
Methods – One hundred twenty-five patients with chronic hepatitis C were included in this study. Patients were investigated using B-mode ultrasound and liver biopsy (Metavir scoring). A texture analysis tool consisting of 12 algorithms and a logistic regression classifier was implemented and validated. Tissue model parameters were varied and ultrasound images were generated.
Results – Texture analysis can discriminate between stages F0 and F4 using actual patient data (accuracy=69.5%) and synthetic images (accuracy=76.6%). A human expert is less sensitive than texture analysis in discriminating subtle changes in ultrasound images. High fibrosis detection accuracies are correlated with larger differences in portal space density (r^2=0.5). Accuracies measured when we varied only the fibrosis stage and kept the rest of the tissue parameters constant showed high detection rates only in a narrow parameter interval.
Conclusion – The texture analysis system shows limited performance in staging fibrosis and it cannot be used for accurate monitoring of fibrosis evolution over time.

Key words
tissue model; fibrosis staging; noninvasive diagnosis; texture analysis

Introduction

Diagnosing liver fibrosis using noninvasive procedures like B-mode ultrasound is challenging because the visual aspects in ultrasound imaging between healthy and fibrotic liver are very much alike. On the other hand, the B-mode ultrasound examination is widely available, can be repeated many times, and is very cost-effective. Hence, there is a constant interest in improving the diagnostic power of B-mode imaging in the field of liver fibrosis. There are several approaches found in the literature. Some authors have evaluated the RF signal [1-2], while others have proposed some visual scores [3-4], but most authors have employed a texture analysis system to discriminate between various fibrosis stages [5-14]. In a recent paper, Bonekamp et al. [15] reviewed current imaging modalities for detecting and staging hepatic fibrosis and cirrhosis. In their review, B-mode ultrasound was mentioned but without any reference to computerized image analysis as being a reliable tool in fibrosis detection. Nevertheless, the most often used method to enhance the diagnostic power of B-mode imaging in the literature is texture analysis. The main assumption of these papers is that fibrosis injuries at the tissue level can produce subtle texture alterations in the ultrasound image. These alterations are not distinguishable with the naked eye, but texture analysis methods can discriminate them, and hence detect fibrotic alterations.

The main goal of this paper is to evaluate this assumption and to investigate the usefulness of a texture analysis tool in direct fibrosis detection and staging. There are two approaches investigated in the current paper. First, a liver tissue model was proposed, and ultrasound images were generated based on this model. The second approach involved a large number of patients who had undergone biopsy and ultrasound examination.

The proposed liver tissue model allowed us to study how various tissue parameters influence the detection rates and to investigate the discrimination power of a human expert with respect to a software analysis tool when detecting certain structures present in the ultrasound image. The tissue model proposed here was built according to relevant histological findings at liver biopsy [16]. The proposed model allowed us to simulate the tissue alterations for each fibrosis stage according to the Metavir scoring system [17]. Although the proposed model could generate all five stages (F0 through F4), the phantom experiments were focused on non-cirrhotic stages (F0-F3).

In the present paper, Field II software was used to generate US images from software phantoms. This software was developed by J.A. Jensen as a fast and accurate method for calculating the pulsed pressure field emitted from an arbitrary shaped, apodized, and excited ultrasound transducer [18-20]. The tissue model was validated by analyzing the statistical properties of the gray levels in the simulated ultrasound image [21]. The textural analysis system implemented here included almost all the textural algorithms encountered in the fibrosis detection literature and was validated against a known set of textures [22]. Texture analysis was applied to a sample size of 125 biopsied patients. The sample size was relatively large when compared to other studies in this field.

There are several major highlights in this paper. The first major contribution is the proposed liver tissue model. The model is accurate enough to capture the microscopic changes that occur during progression of fibrosis. The proposed model can be used to evaluate other noninvasive approaches to fibrosis staging. The second major contribution is the textural analysis system. We implemented a large number of textural algorithms. We also had a large sample size, with over 100 patients being included in the experiments presented in this study.

Material and Methods

Patients and images

This study was approved by the local Ethical Committee of the University of Medicine and Pharmacy, Cluj-Napoca. The patients provided written informed consent before the study began, in accordance with the principles of the Declaration of Helsinki (revision of Edinburgh, 2000).
We prospectively included in this study 125 patients with hepatitis C infection having fibrosis stage 0 or 4 according to the Metavir scoring system. The fibrosis stages were determined by liver biopsy. This sample was selected from 1,200 patients prospectively examined at 3rd Medical Clinic, Cluj-Napoca, Romania, between May 2007 and August 2009. All patients were positive for HCV-RNA and underwent percutaneous liver biopsy (LB) in order to stage and grade their condition. A liver biopsy specimen was taken using the TruCut technique with a Biopty Gun (Bard GMBH, Karlsruhe, Germany) automatic needle device with a diameter of 1.8 mm (14G). The slides were evaluated by a single expert pathologist unaware of the clinical data. The liver fibrosis and necroinflammatory activity were evaluated semi-quantitatively according to the Metavir scoring system [23]. Each patient included in this study underwent an ultrasound examination using a GE Logiq 7 ultrasound machine (General Electric Company, Fairfield, England) with a 5.5-MHz convex phased array probe one day prior to liver biopsy. From each patient were acquired right lobe ultrasound images with liver tissue without blood vessels or other artifacts with a depth setting of 16 cm.
The region of interest (ROI) establishment procedures followed the guidelines presented in the literature [6-8, 11-12, 24-27]. A human expert was instructed to choose one ROI for each patient. The ROI had to be placed as close as possible to the vertical axis of the ultrasound image and at 1 cm below the liver capsule. The ROI had to avoid artifacts and anatomical features like blood vessels, liver capsule, and shadowing, etc. The dimensions of the ROI were 64 x 64 pixels representing an area of 2.62 x 2.62 cm. The expert was a trained radiologist with more than 10 years of experience in gastrointestinal ultrasound investigation.

Liver tissue model

In general, there is a limited number of biopsied patients who can be included in a study. Therefore, the volume of ultrasound images is low. The images are complicated by artifacts due to fat in the abdominal wall, fasting conditions, bowel movement, rib shadows, and blood vessels, etc. The biopsy reading is plagued by expert variability and small sampling volume [28]. As a result, the fibrosis staging is prone to error. The ROI is manually placed by an expert. The position is not fixed with respect to image geometry because the ROI must be set in an artifact-free region. It is known [29] that for a convex probe the point spread function of the system is highly dependent on axial and lateral position in the imaging field. This variation, along with the interpolation operation necessary to display the image, generates a specific texture that overlaps the “texture” produced by the underlying tissue.
In this paper, we propose a liver tissue model that is used in ultrasound image simulations. The tissue model and the simulation setup are designed to meet the shortcomings present in real ultrasound images. The volume of images is limited only by the computation power. The fibrosis staging is a parameter of the tissue model, so it is set beforehand, eliminating the human factor. One can simulate only the desired ROI. This approach eliminates anatomically related artifacts (e.g., blood vessels and rib shadows) and point spread function-related artifacts because the position with respect to the probe is the same for all images. In the present study, we employed a linear aperture instead of a convex one in order to minimize interpolation-related artifacts. Figure 1 shows the difference between a convex probe

and a linear probe. One can see that the local properties of the image are translation invariant only in the case of a linear probe. Of course, the point spread function of the system varies with the position even with a linear aperture.

The liver tissue model was built using relevant quantitative measurements of liver biopsies found in the literature [16]. The following anatomical structures were generated: portal triad (portal space) with the portal vein, fibrous septa, and liver parenchyma consisting of hepatocytes. The model included the healthy liver, fibrosis stages 1, 2, and 3, and cirrhotic liver (F4). In addition, our model can generate a hexagonal grid with different dimensions. This hexagon grid was used in several synthetic experiments. Building of the model starts with a series of points placed in the vertices of a hexagonal grid. This hexagonal grid mimics the shape of the hepatic lobule. The radius of the circumscribed circle for the hexagonal unit is a parameter of the model. Figure 2 shows the hexagon representing the liver lobule. This grid is rotated and translated with a random value. In addition, the position of each point is affected by a normal noise with small standard deviation (SD). We randomly select a number of points. The number of selected points is computed based on the desired portal density. These points establish the position of portal triads. The portal density per mm^2 is another parameter of the model. A Delaunay triangulation [30] is performed on these points, and the resulting edges are kept for later use. Figure 3 shows selected vertices and the triangulated edges.

In each portal triad position is fitted a disc with a random, normally distributed radius. This disc represents the fibrosis naturally occurring inside a portal space. Inside this circle is placed the portal vein. Again, the radius of the portal vein and its position are randomly chosen. Care is taken that the portal vein is inside the portal space. For fibrosis stages greater than 0, the radius of the portal space is progressively increased. In fibrosis stages 1, 2 and 3, fibrous septa are placed around the portal spaces. These septa are placed along the edges obtained after Delaunay triangulation. Each fibrosis stage has several parameters that control the probability of placing a septa, i.e., the mean and SD for the septa length and the septa thickness. In fibrosis stage 4, we place fibrous septa that are spawned along the entire length of the edges. In the liver tissue one can find larger structures, like branch veins and arteries. The walls of these blood vessels bring a significant quantity of fibrous tissue. However, this fibrous tissue has no diagnostic significance in the case of chronic hepatitis C and we did not simulate it.

The parameters for the model variables are given in Table 1 and Table 2. Figure 4 shows several tissue models. For fibrosis stage 4, one should keep in mind that the main features are the fibrous septa that bridge the portal spaces and the regenerative nodules. The dimension of the regenerative nodules depends on the portal density spaces. A low-density value generates a phantom with large areas of "regular" tissue surrounded by thick fibrous septa.

According to Field II specifications, an ultrasound phantom consists of a collection of scatters. We chose a fixed volume inside which we placed a certain number of scatters. The scatters were uniformly distributed inside this volume. The amplitude of each scatter was normally distributed with mean 0 and a certain SD. This standard deviation is referred to as amplitude. This amplitude depended on the underlying anatomical structure. For plain liver tissue, the amplitude was set to 1. If the scatter was inside a vein, the scatter had 0 amplitude (in current implementation the scatter was not generated, in order to improve computation performance). If the scatter was placed on a portal space, or fibrous septa, the amplitude was set to a certain value ≥ 1.

Ultrasound simulation setup

In this section, we will present the simulation setup used to produce ultrasound images. The ultrasound simulation procedure followed the guidelines presented in [18-20]. The tissue phantom was placed

along the X and Z axes (width and depth). Figure 5 shows the simulation setup. On the Y axis (thickness), there are no differences induced by the model; hence, the portal spaces were modeled as cylinders. The physical dimensions of the phantom were width 25.6 mm, depth 25.6 mm, and thickness 5 mm. The phantom was placed under a virtual linear aperture and an ultrasound image was generated. The probe used in this simulation was a 5.5-Mhz linear probe with 98 elements. Apodization was implemented using a Hanning window of 20 active elements. The excitation signal was two wavelengths long. The returned signal was sampled at 100 Mhz. The speed of sound was set at 1540 m/s. In the axial direction, two scatters can be discriminated if they are situated at a distance larger than 1/2 of the pulse width [29]. For the proposed simulation setup, this axial resolution was 0.28 mm:

$$A_r = (N_p \lambda)/2 \quad (1)$$

where A_r is the axial resolution, N_p is the number of wavelengths in the excitation signal, and λ is the wavelength of the ultrasound waves.

There were 25 lines acquired from the underlying medium. Care was taken that all 25 lines were uniformly distributed along the X (width) axis of the phantom. The lateral resolution for the acquisition was 0.97 lines/mm. The envelope of the signal was detected using Hilbert transform. The envelope signal was sampled, logarithmically compressed, and scaled to a 256-level gray scale map. From Equation 1 one can derive the minimum resolution cell than can be resolved by the simulation setup. As a result, the resolution cell for this setup was 0.28 x 0.97 mm^2. However, we assumed a resolution cell of 0.28 x 0.28 mm^2 for density-related computations.

From the RF signals the images were synthesized at a resolution of 5 pixels/mm. At this resolution the physical distance between two pixels was 0.2 mm. This distance was slightly smaller than the theoretical axial resolution for this simulation setup. This ensured that we did not lose information during scan conversion and interpolation. The final image dimension was 128 x 128 pixels. The phantom was placed 30 mm below the ultrasound aperture. In Figure 6 are shown five images corresponding to each of the five fibrosis stages generated using the proposed tissue model.

In [31], the authors established that a large number of scatters could be replaced by a regular grid having a smaller number of scatter points. They also showed that there was no dependence between the number of scatters per resolution cell and the observed speckle pattern. Moreover, in certain conditions the same speckle pattern could be obtained using different underlying scatter distributions. In the present study, 50,000 was chosen as the number of scatters for each phantom . The methods for building an ultrasound phantom with the minimum number of scatters for a certain model is not covered in this paper. Field II simulation software was run on an Intel Pentium D at 3.4 Ghz. In Table 3 are shown the scatter densities and the computation times for various numbers of scatters. We took advantage of both cores; the jobs were distributed by RF lines.

Wagner et al. noted in [21] that the amplitude distribution of a B-mode ultrasound image follows a Rayleigh distribution. This property is used in the ultrasound image simulation literature as a validation method for the simulation setup [31-32]. In the present study, we computed the gray level histogram over several images and compared it with Rayleigh pdf:

$$pdf(x) = \frac{x}{\gamma} e^{-(A^2/2\gamma)} \quad (2)$$

where x is the amplitude and γ is a constant. Two kinds of experiments were performed with the liver tissue model. Synthetic experiments were focused on the study of individual model parameters over the detection rates. These experiments employed the hexagonal grid (Figure 7). Fibrosis detection experiments employed the variability noted in the literature for each model parameter. The detection rates between adjacent fibrosis stages were noted. We investigated in mode detail the impact of portal space density and liver lobule dimensions over the fibrosis stage discrimination. The liver tissue models and the simulation setup were implemented in MATLAB (The MathWorks Inc., Natick, MA)

Texture Analysis

In texture analysis, there are two main steps [33]. The first step is the computation of several textural attributes that numerically describe the texture (using dedicated algorithms). The second step involves the training and evaluation of a classifier using the previously computed textural features. We have provided an overview of each of these two steps as follows.

In the literature, there are many algorithms that describe the texture. Each algorithm treats the texture as being produced by a certain model [33]. There are algorithms that assume the texture as being a collection of pixels having random intensities; other algorithms treat the texture as a superposition of sinusoidal waves with different phases, amplitudes, and frequencies, etc. We selected algorithms that were proposed by various authors for use in fibrosis detection.

Each texture description algorithm has a certain number of parameters that control the feature extraction process. Each algorithm implemented in the present study used the same proposed set of parameters found in corresponding fibrosis detection papers. The following is a list of the algorithms and the papers that use these algorithms in fibrosis detection (when possible): First order statistics [13, 34], gray tone difference matrix [33], gray level co-occurrence matrix [7, 13, 34-35] , multiresolution fractal dimension [7], differential box counting [8, 36], morphological fractal dimension estimators [37], Fourier power spectrum [6-7], Gabor filters [12], Law's energy measures [7], texture edge co-occurrence matrix [8], phase congruency [24], and texture feature coding matrix [14].

Twelve algorithms that process the entire ROI were implemented and 234 features were computed per image. Each image histogram was equalized before entering the feature computation step. This ensured that the detection was not due to some difference in overall gray level. We used logistic regression as a classifier [38]. There are other algorithms that are employed in fibrosis detection, including k-nearest neighbor, neuronal networks, decision trees, and support vector machines, etc. [34]. The reasons for our choice were that logistic regression produces a simple-to-interpret model and does not overfit the data even if the number of instances is lower than the number of features [39-40]. Once the logistic model is generated one can easily study the relevance of the features by looking at the model coefficients. The performance criterion was accuracy, i.e., the ratio between correctly classified instances and the total number of instances in the dataset. To measure the accuracy for a certain dataset the following procedure was applied:

The available data were split into 10 disjointed folds. Iteratively, one fold was used for testing and the other nine for training. The predictions were collected at each step. After 10 steps, the accuracy was computed on all the collected predictions. This process was repeated 10 times with different random splits. The mean accuracy was reported as the performance of the algorithm for the current dataset. Before entering the classification step, each feature was normalized to [0, 1] interval. The test fold subset was also normalized using the same values that were used for the corresponding training set. We recorded only the mean performance and not the variance because cross-validation produces biased variance estimation [41-42].

The texture analysis system was validated using a set of known textures from the Brodatz [43] library. Each image was divided into 100 non-overlapping ROIs. Each ROI had a 64 x 64 pixel area. The textural analysis system was trained to predict the original image from where the ROI originated. The images were chosen according to the guidelines in [22]. Textural algorithms were implemented in a custom-made software system developed at Technical University of Cluj Napoca, Romania. Classification and performance evaluation were implemented using the Weka framework [44] (public domain, ver. 3.7).

Results

Validation of the liver tissue ultrasound image simulation

The simulation setup presented earlier generated 50 images with various tissue parameters. A histogram was computed over this 50 images by summing each histogram bin from individual images. Figure 8 shows the image histogram with the Rayleigh probability distribution function overlapped. The γ parameter (Equation 2) was determined by applying the maximum likelihood algorithm to the amplitude values. One can easily see that the proposed setup behaved as expected.

Validation of the textural analysis system

The texture analysis system was validated using three sets of images. The first dataset contained regions from D77, D84, D55, D53, and D24 Brodatz textures. The second dataset consisted of D4 and D84 textures. The third set had regions from D5 and D92. The classification accuracy was 98.9 for the first set, 98.4 for the second set, and 97.9 for the third set. The image combinations applied here are three of the image sets employed by Randen et al. [22] to evaluate several texture analysis algorithms. These image sets covered binary and multiclass classification problems.

Fibrosis detection in hepatitis C patients

The fibrosis stage distribution in our patients was as follows: F0 –51 (40.8%) and F4 – 74 (59.2%). Figure 9 shows several portal spaces with various fibrosis stages. On average, 12.94 (standard deviation: 6.69) right lobe ultrasound images were acquired from each patient. The radiologist established 122 ROIs, one for each patient, as shown in Figure 10. There were three patients with poor quality images in whom the radiologist was not able to establish a ROI. Two were healthy patients and one cirrhotic. Each ROI was labeled according to Metavir findings and processed by means of texture analysis. Texture analysis was trained to predict the fibrosis stage of the patient (F0 or cirrhotic – F4). The overall recorded accuracy was 69.5%.

Synthetic experiments on liver tissue models

Experiment 1. In this experiment, we compared the discrimination power of the human expert versus the accuracy of the texture analysis. The following experiment was designed. Using the hexagonal grid model several sets of images were generated. Each set had 50 images. The hexagonal grid radius was set to 6 mm, and 50,000 scatters were generated per phantom. There were two parameters that were varied. First, the amplitude was varied between 1 and 4 in steps of 0.1. A set was generated for each amplitude value. The thickness of the hexagon edge was set to 0.3 mm. The other tested parameter was the edge thickness. With the amplitude set to 3, the thickness was set between 0.01 and 0.35 mm with various steps. Five images were extracted from some of the amplitude sets and some of the thickness sets. These images were shown to two radiologists. The experts were instructed to note when they observed a hexagonal grid on the images. They were told that the grid dimensions were the same but the position would vary for each image. They were not told the expected number of images with the hexagonal grid. Before the experiment began, they visualized several examples of hexagonal grid images with a high amplitude (5) and 0.5 mm grid thickness (Figure 7). The results are shown in Figure 11 and Figure 12. Because the human expert is a scarce resource, we were not able to test the entire spectra of values.

Experiment 2. In this experiment, we varied the fibrosis stage and the two main parameters, portal space density and portal lobule dimensions. The values for portal space density were 0.1, 0.34, 0.58, 0.82, 1.07, 1.31, 1.55, and 1.8 portal spaces/mm^2. The values for lobule radius were 0.4, 0.51, 0.63, and 0.75 mm. A 50-image set was generated from each combination of fibrosis stage (F0-F3), portal density, and lobule radius. For this experiment, we generated 6,400 phantoms.

Each fibrosis stage was paired with the next stage. Among adjacent fibrosis stages, all possible parameter combinations were grouped in two class problems. A classifier was trained for each pair and the accuracy was determined. The correlation rates of the detection accuracy with each of the model parameters are shown in Table 4.

From the same experiment, we selected only cases where the two tissue parameters were the same. These comparison cases could be found when we employed the noninvasive staging tool to observe the fibrosis evolution for the same patient over time. We assumed that the portal density space and lobule dimensions remained constant for a specified patient. Graphs representing the detection accuracy for each parameter combination are shown in Figure 13 through Figure 15. Again, we grouped adjacent fibrosis stages.

Fibrosis detection in liver tissue models

Experiment 3. In this experiment, we investigated the fibrosis detection rates when the liver lobule dimensions and portal space density varied. Each phantom was generated using random values for these two parameters. There were two experiments, one with uniformly distributed values in +- 2 SD from mean and another one with normally distributed values. The values for the mean and standard deviations were set according to histological findings (see Table 1 and Table 2). Eight hundred images were generated from each fibrosis stages (F0-F4). The results are shown in Figure 16. One should note a sharp drop in performance when discriminating between F2 and F3. We also investigated the discrimination accuracy between the F0 model and F4 model in order to match the actual patient data. The overall recorded accuracy was 74.2% for uniformly distributed parameters and 76.6% for normally distributed parameters.

Discussion

The ultrasound simulation field is a rich one. The main applications are focused on cardiovascular imaging or simulation of ultrasound imaging from CT data, but there are approaches to ultrasound image segmentation and registration, etc.

In [45], the authors showed that there are several tools available to simulate ultrasound images. The authors pointed out that the realism of the simulation cannot be achieved without computational effort. After analyzing several commercial and noncommercial ultrasound simulation systems, the authors in [46] claimed that the Field II package [18] yields the best results with a carefully designed phantom, but this method has the disadvantage of being very slow. In a recent review [47] focused on ultrasound image segmentation, the authors referred to the Field II software package as an effective application for producing ground truth data. There are other approaches that relate to the Field II package. In [32], the authors proposed a faster, convolution-based system that simulates 2D/3D cardiac images. The authors showed that the generated images had the same Rayleigh statistics and the same visual aspects as those of Field II-generated images. In [31], the authors investigated phantom complexity-related issues and presented means of reducing the number of scatters and the computational time.

The most important part of an ultrasound simulation system is the ultrasound phantom. Again, most of the papers are focused on the cardiovascular system. Ultrasound liver imaging has received less attention. In [48], the authors proposed a software liver phantom that was focused mainly on other liver diseases like steatosis. The features they used were built around the concept of attenuation. In [49], the authors proposed a liver phantom that was then used to study the modifications of speckle distribution in cirrhosis. They proposed a tissue model that consisted of a reticular structure with high scattering properties. Inside this structure were regions with low scattering properties (mimicking the regenerative nodules). In [50], the same authors proposed a software phantom that could reproduce the statistical distributions of fibrosis. The phantoms presented in the literature accounted for fibrosis in a statistical manner. To our knowledge, there are no software phantoms that mimic the microscopic structure of liver tissue in as much detail as our proposal.

The tissue model proposed here includes the most important features of liver tissues that can be found at the microscopical level. The dimensions of these structures are set according to relevant quantitative measurements encountered in the literature [16]. The alterations due to fibrosis were modeled according to Metavir score. Figure 9 shows several portal spaces affected by various stages of fibrosis due to hepatitis C infection. Figure 4 shows the proposed tissue model mimicking the fibrosis distribution in each stage. The parameters of the proposed model allow the user to vary the patient characteristics such as portal space density, radius of a liver lobule, and dimensions of the portal space. The portal space density was expressed in portal spaces per mm^2 instead of mm^3 because when evaluating a liver biopsy the physician counts the number of portal spaces found on a certain biopsy. At biopsy, the tissue is prepared as a series of thin slices; hence, they measure the area instead of the volume. The present model can be adapted to match other fibrosis scoring systems.

Textural analysis on B-mode ultrasound follows four main steps. First, a physician acquires a right lobe ultrasound image. Then, another physician (or the same one) establishes a rectangular ROI on the ultrasound image. For fibrosis detection, most authors suggest that the ROI should be placed in a homogenous area, avoiding artifacts and anatomical features like blood vessels, liver capsule, and rib shadows. In the present liver model, we considered the ideal case, i.e., the absence of such structures in the simulated regions. In the remaining steps, the texture analysis is employed and detection rates are computed. It is important to note that the simulation setup presented here eliminated the need for a human expert and thus eliminated the operator-dependent variability that is present in the first two steps of the classical approach.

Discussions regarding performance evaluation methodology and user variability introduced by the experts are beyond the scope of this paper; however, these are issues that need attention because a permissive methodology might yield positively biased performance estimations.
Another clear advantage to the simulation setup is that there are no constraints regarding patient availability. The volume of data is limited only by the computational power. The drawbacks of the approach presented here are that the liver tissue model might not be accurate enough and the variability introduced in the model might not match the variability present in an actual population. Another limitation is that the ultrasound simulation step requires a lot of processing time.
The experiments presented here tested the main assumption of direct fibrosis detection by means of texture analysis. The assumption is that fibrosis alterations at the liver lobule level can induce significant changes in the speckle pattern of the ultrasound image. Even if these alterations are not visible with the naked eye, a texture analysis system can detect and learn these alterations.
From Figure 11 and Figure 12 of the first experiment, one can observe that the software system outperformed the "performance" of the human expert. The test could be more accurate if we instructed the physicians to mark the hexagonal grid on the images. Unfortunately, this is a very time-consuming activity and the experts were not available for this activity. The texture analysis system was more sensitive to the presence of certain structures in the underlying medium than the human eye. However, one can see that there are limitations in detection rates even for the texture analysis system. These findings endorse the assumption that a texture analysis tool is more sensitive to ultrasound texture alterations than a human expert.
The second experiment was conducted to study performance with respect to various tissue parameters. The detection rates depended heavily on the physical parameters of the phantom. An interesting finding was that a low portal density for the lower fibrosis stage was correlated with high detection rates. In a similar fashion, a greater difference in the portal density value between the two lots correlated with greater detection rates. One can note that in a lower fibrosis stage there is less fibrosis. At the same time, a lower density value translates into fewer portal spaces and again in a lower fibrosis quantity in the tissue. The other parameter, the liver lobule radius, does not have an impact on detection rates. The data gathered from this experiment indicated that the textural analysis is more sensitive to the variation in the portal space density than to the variation in fibrosis stage. Moreover, the detection rates correlated with differences in the amount of fibrosis present in the liver tissue and not with the distribution of the fibrosis (as presented in Table 4).
The second part of experiment 2 studied the performance when we employed the noninvasive staging tool to observe fibrosis evolution in the same patient over time. One can note that higher detection rates are obtained only for a small parameter domain. Even these values are not high enough to be considered for clinical practice. We concluded that textural analysis cannot be used as an accurate noninvasive instrument to observe fibrosis evolution over time. This result was rather disappointing because such a tool could be very useful in clinical practice.
The results obtained from experiment 3 (Figure 16) showed low detection rates when the texture analysis was trained to discriminate between adjacent fibrosis stages. The findings presented in the simulation section do not endorse the assumption that the liver fibrosis in chronic hepatitis C produces significant alterations of the ultrasound speckles, alterations that can be directly detected by means of textural analysis.
The detection performance on actual patient data was lower than the accuracy recorded on the simulated images. Expert variability at biopsy interpretation, at ultrasound examination, and at the establishment of the ROI could contribute to lower detection rates in patient images. On the other hand, there is the possibility that the variation in tissue parameters reported by the authors in [16] is much larger.

There are other possibilities, less explored in the literature, for B-mode ultrasound-based fibrosis staging. Some authors have proposed fibrosis detection using several visual scores [3-4]. These scores are quantified by a trained physician. Unsupervised quantification of the visual scores could be more effective in staging or tracking the fibrosis evolution because they quantify the ultrasound image alterations that are indirectly produced by fibrosis. Other authors have studied the properties of the reflected RF signal, properties like attenuation [51], backscatter [52], or statistical properties [9, 49-50, 53]. The tissue phantom presented here can be applied to optimize these methods. The speed of the simulation can be improved by employing scatter equivalence introduced in [31]. The liver tissue model can be improved by further quantitative studies on liver biopsies.

This paper brings several contributions to the noninvasive diagnosis field. To our knowledge, the liver tissue model introduced here has the most accurate representation of actual liver structures encountered at the microscopic level. The number of patients included in the present paper (over 120) is relatively large when compared to other studies in this field. Gaitini et al. [26] included 44 patients, Li et al. [5] included six patients, Cao et al. [8, 25] included 36 patients, Horng et al. [27] included 40 patients, Yeh et al. [35] included 20 fresh human liver samples obtained from surgical specimens, Badawi et al. [13] included 140 patients, Mojsilovic et al. [11] included 30 patients, Kadah et al. [34] included 120 patients, Abe et al. [6] included 22 patients, and Wu et al. [7] included 45 patients. Other authors did not report the number of patients, only the number of images [10, 12, 14, 24, 36]. Our textural analysis system included almost all of the textural algorithms encountered in the fibrosis detection literature.

Conclusions

In the present paper, we proposed a liver tissue model and evaluated noninvasive fibrosis detection from B-mode ultrasound images by means of texture analysis. The proposed liver tissue model is a reliable tool for investigating noninvasive fibrosis staging and detection methods. The model is presented in enough detail to allow easy implementation. The model parameters have been established following quantitative liver biopsy measurements and are fully presented throughout the paper.
The major findings from the experiments performed here are that the texture analysis methods have superior discrimination powers compared to human experts. At the same time, texture analysis tools are not useful in accurate direct fibrosis detection. This is true for transversal and longitudinal studies. It is safe to conclude that the prediction of Metavir fibrosis stage cannot be accurately made using textural analysis because textural analysis is more sensitive to the overall quantity of fibrosis and various tissue parameters than to the quality and distribution of the fibrosis at the hepatic lobule level. Findings from the actual patient population endorse this conclusion.

Acknowledgements

Part of this work was funded by National Council for Scientific Research in Higher Education Grant No. 41-071/2007: SONOFIBROCAST.

References

1) Oosterveld B, Thijssen M, Romijnt R. Ultrasound attenuation and texture analysis of diffuse liver disease: methods and preliminary results. Phys Med. 1991;36:1034-64.
2) Fujii Y, Taniguchi N, Wang Y, et al. Clinical application of a new method that segments the region of interest into multiple layers for RF amplitude histogram analysis in the cirrhotic liver. Journal of Medical Ultrasonics. 2004;31:91-8.
3) Saverymuttu SH, Joseph AE, Maxwell JD. Ultrasound scanning in the detection of hepatic fibrosis and steatosis. Br Med J (Clin Res Ed). 1986 Jan 4;292:13-5.
4) Colli A, Fraquelli M, Andreoletti M, et al. Severe liver fibrosis or cirrhosis: accuracy of US for detection--analysis of 300 cases. Radiology. 2003 Apr;227:89-94.
5) Li GD, Min LQ, Zang HY, et al. Some information of B-Scan image that detected by CNN. 2006 IEEE International Conference on Information Acquisition, Vols 1 and 2, Conference Proceedings. 2006:819-23.
6) Abe C, Kahn CE, Jr., Doi K, et al. Computer-aided detection of diffuse liver disease in ultrasound images. Invest Radiol. 1992 Jan;27:71-7.
7) Wu CM, Chen YC, Hsieh KS. Texture Features for Classification of Ultrasonic Liver Images. Ieee T Med Imaging. 1992 Jun;11:141-52.
8) Cao GT, Shi PF, Hu B. Liver fibrosis identification based on ultrasound images captured under varied imaging protocols. J Zhejiang Univ Sci B. 2005 Nov;6:1107-14.
9) Yamada H, Ebara M, Yamaguchi T, et al. A pilot approach for quantitative assessment of liver fibrosis using ultrasound: preliminary results in 79 cases. J Hepatol. 2006 Jan;44:68-75.
10) Jeong JW, Lee S, Lee JW, et al. The echotextural characteristics for the diagnosis of the liver cirrhosis using the sonographic images. P Ann Int Ieee Embs. 2007:1343-5.
11) Mojsilovic A, Popovic M, Markovic S, et al. Characterization of visually similar diffuse diseases from B-scan liver images using nonseparable wavelet transform. Ieee T Med Imaging. 1998 Aug;17:541-9.
12) Ahmadian A, Mostafa A, Abolhassani MD, et al. A texture classification method for diffused liver diseases using Gabor wavelets. 2005 27th Annual International Conference of the IEEE Engineering in Medicine and Biology Society. 2005;1-7:1567-70.
13) Badawi AM, Derbala AS, Youssef AM. Fuzzy logic algorithm for quantitative tissue characterization of diffuse liver diseases from ultrasound images. Int J Med Inform. 1999 Aug;55:135-47.
14) Horng M-H, Sun YN, Lin XZ. Texture feature coding method for classification of liver sonography. Computerized Medical Imaging and Graphics. 2002 Jan-Feb;26:33-42.
15) Bonekamp S, Kamel I, Solga S, et al. Can imaging modalities diagnose and stage hepatic fibrosis and cirrhosis accurately? J Hepatol. 2009 Jan;50:17-35.
16) Crawford AR, Lin XZ, Crawford JM. The normal adult human liver biopsy: a quantitative reference standard. Hepatology. 1998 Aug;28:323-31.
17) Bedossa P, Poynard T. An algorithm for the grading of activity in chronic hepatitis C. The METAVIR Cooperative Study Group. Hepatology. 1996 Aug;24:289-93.
18) Jensen J, Munk P. Computer phantoms for simulating ultrasound B-mode and cfm images. Acoustical Imaging. 1997;23:75-80.
19) Jensen J. Field: A program for simulating ultrasound systems. Medical and Biological Engineering and Computing. 1996;34:351-2.

20) Jensen J, Svendsen N. Calculation of pressure fields from arbitrarily shaped, apodized, and excited ultrasound transducers. IEEE Transactions on Ultrasonics, Ferroelectrics and Frequency Control. 1992;39:262-7.
21) Wagner R, Smith S, Sandrik J, et al. Statistics of speckle in ultrasound B-scans. Ieee Trans Sonics Ultrasonics. 1983;30:156-63.
22) Randen T, Husoy JH. Filtering for texture classification: A comparative study. Ieee T Pattern Anal. 1999 Apr;21:291-310.
23) Intraobserver and interobserver variations in liver biopsy interpretation in patients with chronic hepatitis C. The French METAVIR Cooperative Study Group. Hepatology. 1994 Jul;20:15-20.
24) Cao G, Shi P, Hu B. Ultrasonic Liver Characterization Using Phase Congruency. Proc 27th Ann Int Conf IEEE-EMBS 2005 Jan.:6356-9.
25) Cao GT, Shi PF, Hu B. Liver fibrosis identification based on ultrasound images. 2005 27th Annual International Conference of the IEEE Engineering in Medicine and Biology Society, Vols 1-7. 2005:6317-20.
26) Gaitini D, Baruch Y, Ghersin E, et al. Feasibility study of ultrasonic fatty liver biopsy : texture vs. attenuation and backscatter. Ultrasound Med Biol. 2004 Oct;30:1321-7.
27) Horng M-H. An ultrasonic image evaluation system for assessing the severity of chronic liver disease. Computerized Medical Imaging and Graphics. [doi: DOI: 10.1016/j.compmedimag.2007.05.001]. 2007;31:485-91.
28) Bedossa P, Dargere D, Paradis V. Sampling variability of liver fibrosis in chronic hepatitis C. Hepatology. 2003;38:1449-57.
29) Jan J. Medical image processing, reconstruction, and restoration: concepts and methods. CRC, editor. Boca Raton,FL: Taylor & Francis Group; 2006.
30) De Berg M, Cheong O, Van Kreveld M, et al. Delaunay Triangulations. Computational geometry: algorithms and applications: Springer-Verlag New York Inc; 2008. p. 386.
31) Dantas RG, Costa ET, Leeman S. Ultrasound speckle and equivalent scatterers. Ultrasonics. 2005 May;43:405-20.
32) Gao H, Choi H, Claus P, et al. A fast convolution-based methodology to simulate 2D/3D cardiac ultrasound images. IEEE Transactions on Ultrasonics, Ferroelectrics and Frequency Control. 2009;56:404-9.
33) Materka A, Strzelecki M. Texture analysis methods a review: Technical University of Lodz, Institute of Electronics,1998.
34) Kadah YM, Farag AA, Zurada JM, et al. Classification algorithms for quantitative tissue characterization of diffuse liver disease from ultrasound images. Ieee T Med Imaging. 1996 Aug;15:466-78.
35) Yeh WC, Huang SW, Li PC. Liver fibrosis grade classification with B-mode ultrasound. Ultrasound Med Biol. 2003 Sep;29:1229-35.
36) Lee W, Hsien K, Chen Y. A study of ultrasonic liver images classification with artificial neural networks based on fractal geometry and multiresolution analysis. Biomedical Engineering - Applications, Basis&Communications. 2004;16:17-25.
37) Xia Y, Feng DG, Zhao RC. Morphology-based multifractal estimation for texture segmentation. Ieee T Image Process. 2006 Mar.;15:614-23.
38) Friedman J, Hastie T, Tibshirani R. The elements of statistical learning: Springer Series in Statistics; 2001.
39) Landwehr N, Hall M, Frank E. Logistic model trees. Mach Learn. 2005 May;59:161-205.
40) Friedman J, Hastie T, Tibshirani R. Additive logistic regression: A statistical view of boosting. Ann Stat. 2000 Apr;28:337-74.

41) Grandvalet Y, Bengio Y. Hypothesis Testing for Cross-Validation. Montreal Universite de Montreal, Operationnelle DdIeR;2006 August 29th Contract No.: 1285.
42) Bengio Y, Grandvalet Y. No unbiased estimator of the variance of k-fold cross-validation. The Journal of Machine Learning Research. 2004;5:1089-105.
43) Brodatz P. Textures: A Photographic Album for Artists and Designers.: Dover, New York; 1966.
44) Witten I, Frank E. Data Mining: Practical machine learning tools and techniques: Morgan Kaufmann Pub; 2005.
45) Reichl T, Passenger J, Acosta O, et al. Ultrasound goes GPU: real-time simulation using CUDA. Procs SPIE. 2009.
46) Kutter O, Shams R, Navab N. Visualization and GPU-accelerated simulation of medical ultrasound from CT images. Comput Methods Programs Biomed. 2009 Jun;94:250-66.
47) Noble JA, Boukerroui D. Ultrasound image segmentation: A survey. Ieee T Med Imaging. 2006 Aug;25:987-1010.
48) Zatari D, Botros N, Dunn F. A simulation algorithm for ultrasound liver backscattered signals. Ultrasonics. 1995 Nov;33:469-74.
49) Yamaguchi T, Hachiya H. Modeling of the Cirrhotic Liver Considering the Liver Lobule Structure. Jpn J Appl Phys. 1999;38:3388-92.
50) Yamaguchi T, Hachiya H. Proposal of a parametric imaging method for quantitative diagnosis of liver fibrosis. Journal of Medical Ultrasonics [serial on the Internet]. 2010 July [cited 2010 06 Aug]: [about 12 p.]. Available from: http://dx.doi.org/10.1007/s10396-010-0270-y.
51) Szebeni A, Tolvaj G, Zalatnai A. Correlation of ultrasound attenuation and histopathological parameters of the liver in chronic diffuse liver diseases. Eur J Gastroen Hepat. 2006 Jan;18:37-42.
52) Machado CB, Pereira WCD, Meziri M, et al. Characterization of in vitro healthy and pathological human liver tissue periodicity using backscattered ultrasound signals. Ultrasound Med Biol. 2006 May;32:649-57.
53) Nakajima S, Shibuya K, Kamiyama N, et al. Comparison of ultrasound colored image views produced by application of statistical analysis of radio-frequency signals and histological findings in patients with chronic hepatitis C. Journal of Medical Ultrasonics. 2010;37:51-8.

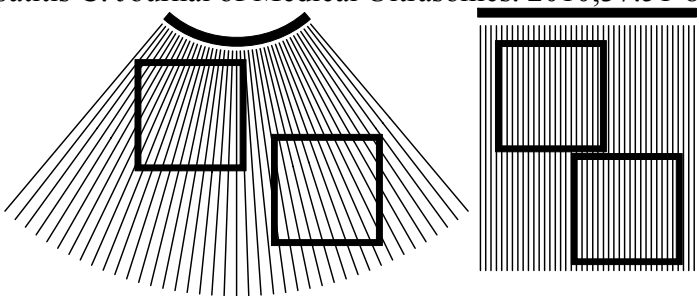

Figure 1. Convex array (left) vs. linear array (right). Pixel intensities are computed along the A lines (thin lines). The rest of the pixels are interpolated. The thick rectangles represent the region of interest. In the case of the convex array, one can note different image properties when this region of interest is moved. In the case of the linear probe, different positions yield the same image properties.

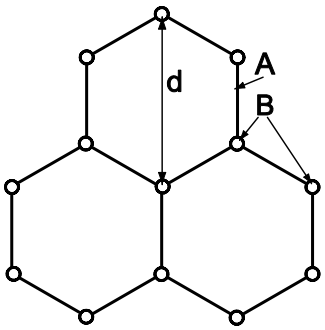

Figure 2. Hexagonal grid with three adjacent liver lobules. (a) Liver lobule boundary. (b) Portal space. (d) Liver lobule diameter.

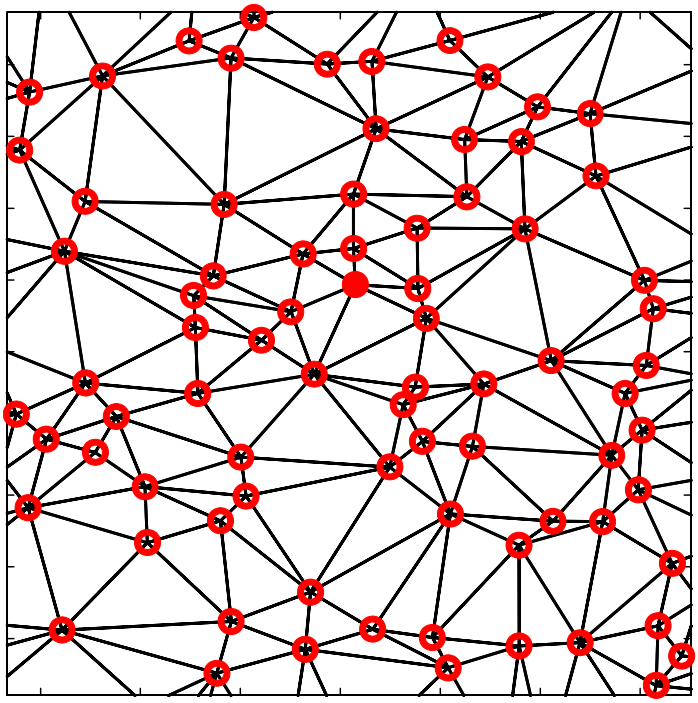

Figure 3. Portal spaces (red circles) and the Delaunay edges. The fibrosis is placed along these edges. One should note that these edges extend also to portal spaces outside the simulated region, like in real liver tissue.

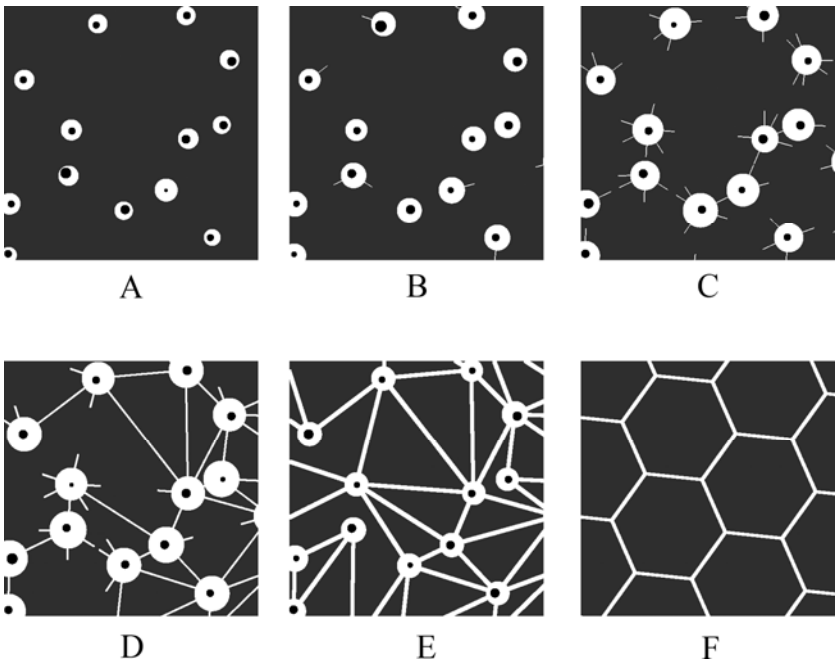

Figure 4. Examples of tissue simulations for each of the model types. (a)-(e) Fibrosis stages 0 through 4. (f) Hexagonal grid used in synthetic tests. Each image is 5.12 x 5.12 mm and is taken from the same position. The position of the portal spaces is identical in the five images.

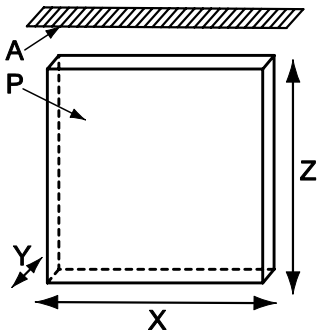

Figure 5. Simulation setup. The phantom (p) is placed under a linear aperture (a). Note the axis convention, where Z is perpendicular to the aperture and X is parallel to the length of the aperture.

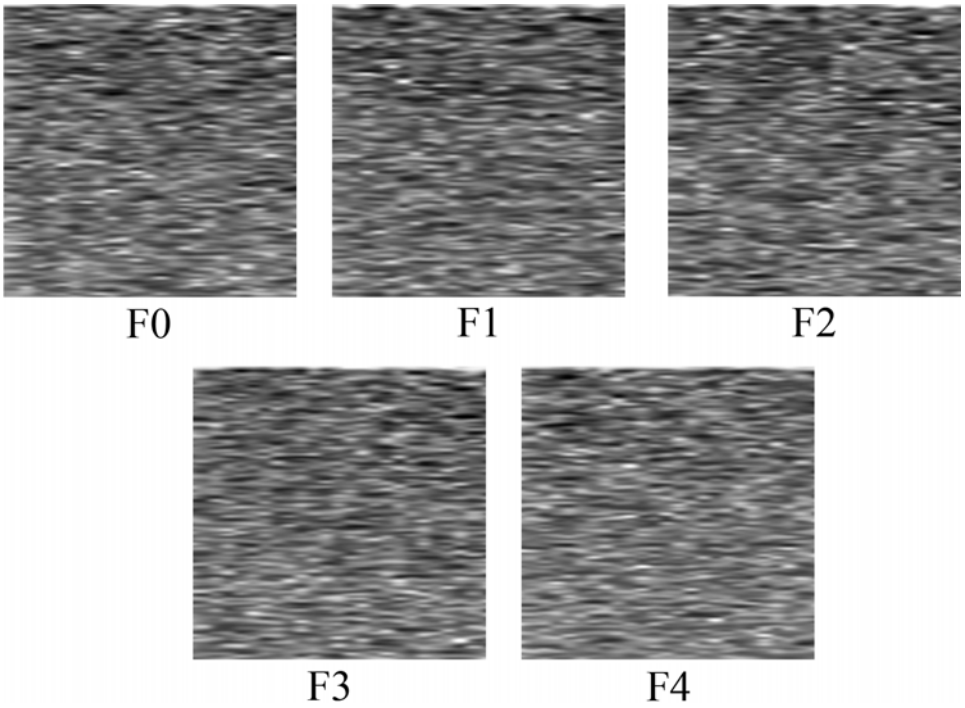

Figure 6. Ultrasound images generated from F0 through F4 fibrosis tissue models. One can note that the visual aspects of these images are very much alike. The random number generator that selected the portal triads was initialized with the same value for all five phantoms. As a result, the position of the portal spaces is the same in all five phantoms.

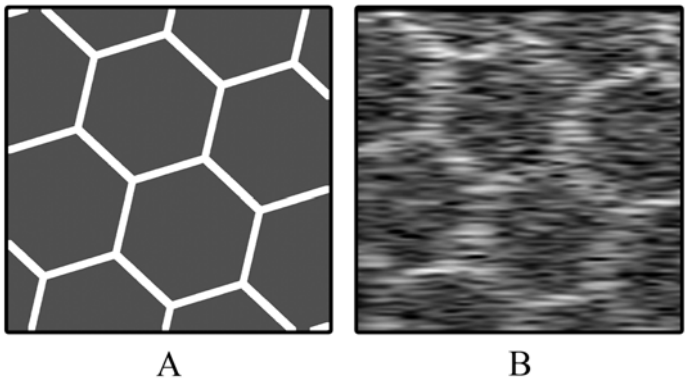

Figure 7. Hexagonal tissue model (a) and generated ultrasound image (b).

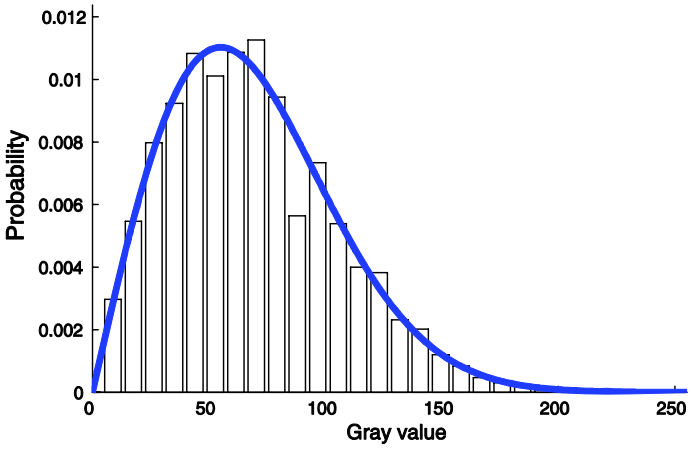

Figure 8. Statistics of the simulated images. The bars represent the image histogram and the thick blue line the fitted Rayleigh distribution.

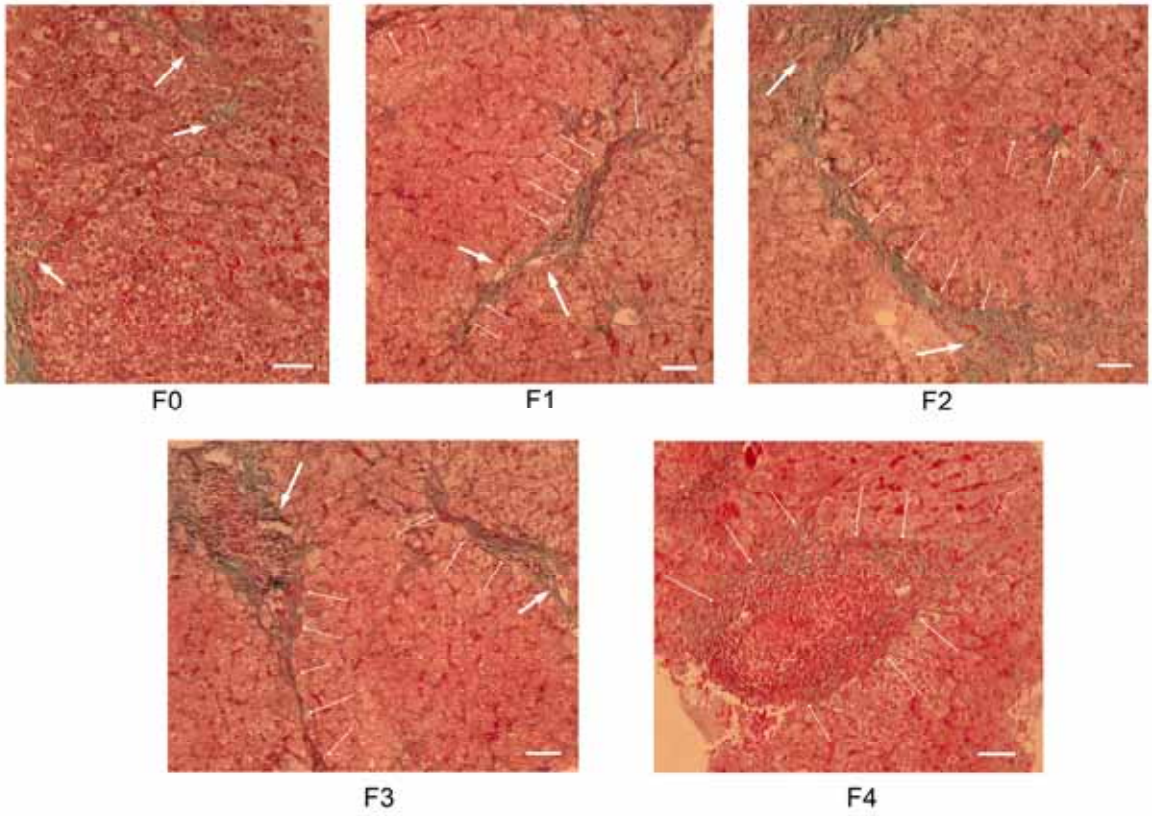

Figure 9. Examples of portal spaces with various fibrosis stages. F0: healthy liver, F1-F3: fibrosis stages 1 through 3, F4: regenerative nodule from a cirrhotic liver. Thick arrows show the portal spaces. Thin arrows show the fibrous septa. The horizontal bar represents 100 μm.

Figure 10. Left lobe liver ultrasound image. The rectangle shows the 64 x 64-pixel region of interest.

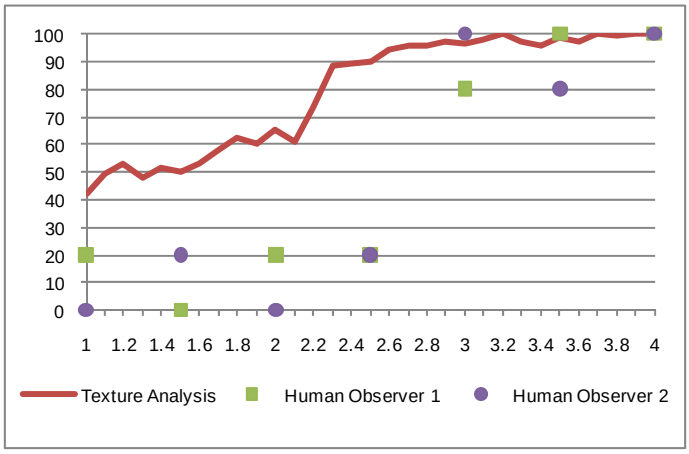

Figure 11. Comparison between discrimination performance of the human experts and texture analysis system. The amplitude of the model is varied. The rest of the parameters remain unchanged. The Y coordinate represents accuracy (%). The X coordinate represents the amplitude.

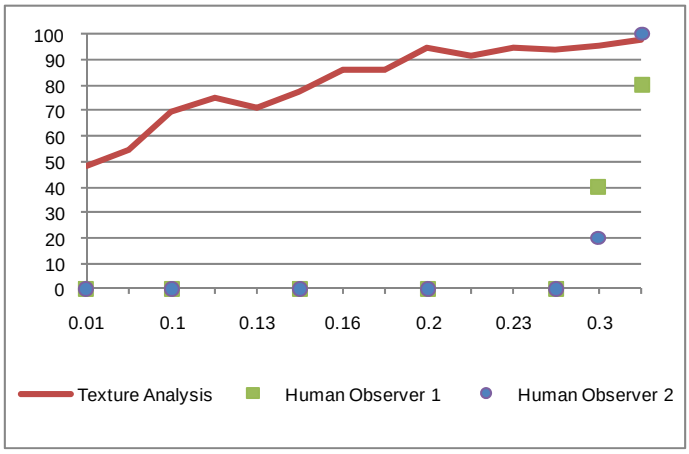

Figure 12. Comparison between discrimination performance of the human experts and texture analysis system. The thickness of the hexagonal grid is varied. The rest of the parameters remain unchanged. The Y coordinate represents accuracy (%). The X coordinate represents the thickness in mm.

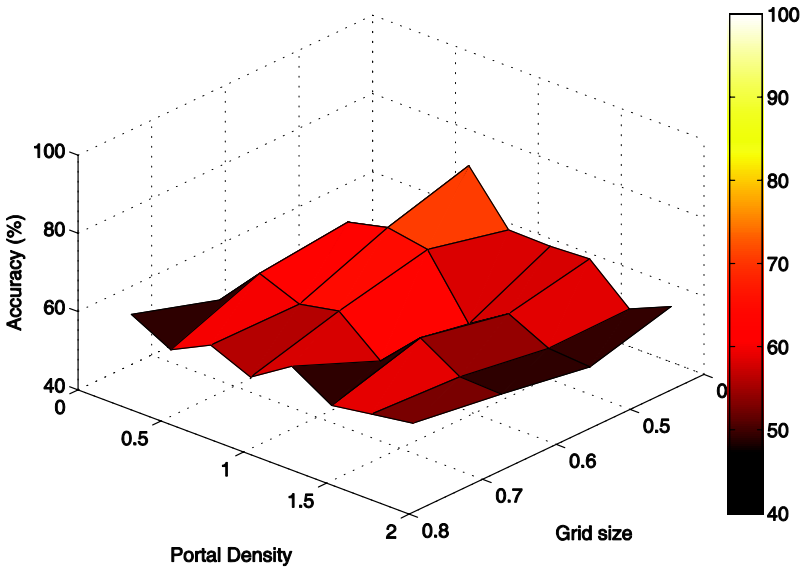

Figure 13. Detection rates between F0 and F1 stages when the model parameters are kept constant throughout the matching datasets. All 8 x 4 parameter combinations generated a dataset.

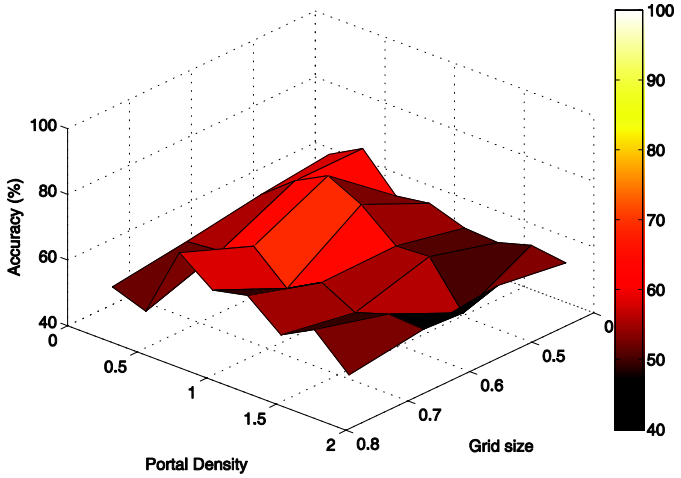

Figure 14. Detection rates between F1 and F2 stages when the model parameters are kept constant throughout the matching datasets. All 8 x 4 parameter combinations generated a dataset.

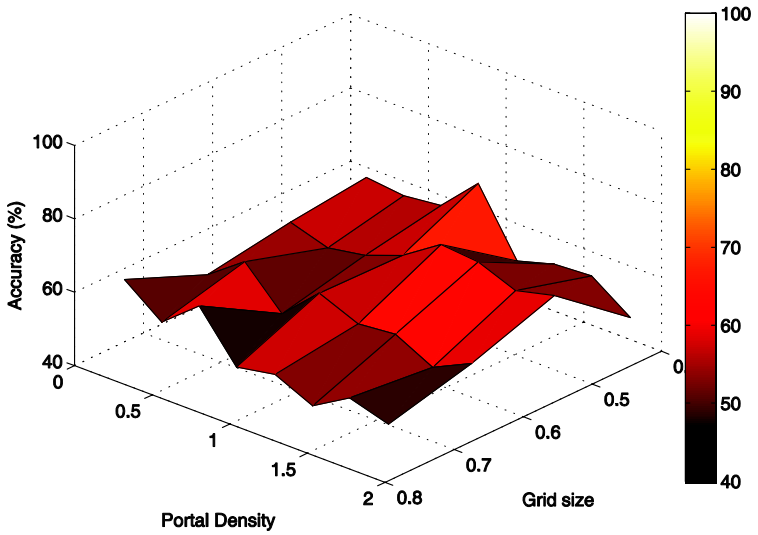

Figure 15. Detection rates between F2 and F3 stages when the model parameters are kept constant throughout the matching datasets. All 8 x 4 parameter combinations generated a dataset.

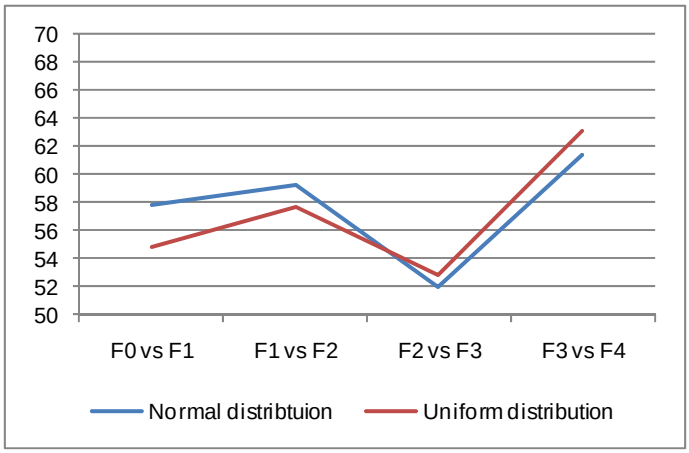

Figure 16. Detection rates when discriminating between adjacent fibrosis stages. The Y scale represents accuracy (%). The detection rates behave identically regardless of the normal/uniform variable distribution.

Table 1. Model variables for healthy human liver. Portal density is evaluated as seen at the liver biopsy.

Parameter	Mean	Standard Deviation
Radius of the hexagonal cell (mm)	1.15	0.11
Portal density (portal spaces/mm^2)	0.8	0.5
Radius of the healthy portal space (mm)	0.2	0.015
Radius of the portal vein (mm)	0.08	0.015

Table 2. Model variables for fibrosis stages greater than 0. The radius of the portal space and septa length, etc., are randomly chosen for each individual portal space. Occurrence probabilities are fixed for the model.

Parameter	**Fibrosis 1**		**Fibrosis 2**		**Fibrosis 3**		**Fibrosis 4**	
	Mean	SD	Mean	SD	Mean	SD	Mean	SD
Radius of the portal space (mm)	0.25	0.015	0.3	0.015	0.35	0.015	0.25	0.015
Length of a septa (mm)	0.45	0.015	0.55	0.015	0.6	0.015	N/A4	N/A
Thickness of a septa (mm)	0.02	0.0008	0.02	0.0008	0.02	0.0008	0.105	0.015
Probability of a septa	0.05	N/A	0.9	N/A	0.9	N/A	0	N/A
Probability of a bridging septa	0	N/A	0	N/A	0.4	N/A	1	N/A

Table 3. Computation times and densities for different numbers of scatters. The scatter density is computed after projecting the whole phantom on the XZ plane. The total area of the phantom projection is 25.6 x 25.6 mm^2. The resolution cell is assumed to be 0.28 x 0.28 mm^2. Computation times are evaluated for a single core.

Number of scatters	**Scatter density per mm^2**	**Scatter density per resolution cell**	**Computation time per phantom (seconds)**
10000	15.2	1.19	50
17000	25.9	2.03	75
30000	45.7	3.58	150
50000	**76.2**	**5.98**	**250**
100000	152.5	11.96	500
300000	457.7	35.88	1475
500000	762.9	59.81	2575
1000000	1525.9	119.63	5150

Table 4. Correlation coefficients between accuracy of detection and each of the model parameters. The datasets group adjacent fibrosis stages. For each dataset we have two sets of parameters, one for the lower fibrosis stage and the other for the higher fibrosis stages. The correlation was also computed with respect to the absolute difference between the model parameters.

	Lower fibrosis stage		**Higher fibrosis stage**			
Comparison case	**Radius of hexagonal cell**	**Portal density**	**Radius of hexagonal cell**	**Portal density**	**Difference of radius**	**Difference of portal density**
F0 - F1	0.031	**-0.558**	-0.062	0.165	0.001	**0.504**
F1 - F2	0.041	**-0.468**	-0.057	-0.083	0.023	**0.466**
F2 - F3	0.034	**-0.421**	-0.033	-0.058	0.0191	**0.414**